

Large-area synthesis of nanoscopic catalyst-decorated conductive MOF film using microfluidic-based solution shearing

Jin-Oh Kim

Korea Advanced Institute of Science and Technology <https://orcid.org/0000-0002-3322-7100>

Won-Tae Koo

Korea Advanced Institute of Science and Technology

Hanul Kim

Korea Advanced Institute of Science and Technology <https://orcid.org/0000-0003-3183-8917>

Chungseong Park

Korea Advanced Institute of Science and Technology

Calvin Hutomo

Korea Advanced Institute of Science and Technology

Siyong Q. Choi

Korea Advanced Institute of Science and Technology

Il-Doo Kim

Korea Advanced Institute of Science and Technology <https://orcid.org/0000-0002-9970-2218>

Steve Park (✉ stevepark@kaist.ac.kr)

Korea Advanced Institute of Science and Technology

Article

Keywords: Conductive metal-organic frameworks, Microfluidic, Solution shearing, Gas sensors

Posted Date: January 18th, 2021

DOI: <https://doi.org/10.21203/rs.3.rs-124035/v1>

License: © ⓘ This work is licensed under a Creative Commons Attribution 4.0 International License.

[Read Full License](#)

Version of Record: A version of this preprint was published at Nature Communications on July 13th, 2021. See the published version at <https://doi.org/10.1038/s41467-021-24571-1>.

Large-area synthesis of nanoscopic catalyst-decorated conductive MOF film using microfluidic-based solution shearing

Jin-Oh Kim^{1,4}, Won-Tae Koo^{1,2,4}, Hanul Kim³, Chungseong Park^{1,2}, Calvin Andreas Hutomo¹, Siyoung Choi³, Il-Doo Kim^{1,2} and Steve Park¹

¹ Department of Materials Science and Engineering, Korea Advanced Institute of Science and Technology (KAIST), 291 Daehak-ro, Yuseong-gu, Daejeon 34141, Republic of Korea

² Membrane Innovation Center for Anti-virus & Air-quality Control, KAIST Institute for Nanocentury, 291, Daehak-ro, Yuseong-gu, Daejeon 34141, Republic of Korea

³ Department of Chemical and Biomolecular Engineering, Korea Advanced Institute of Science and Technology (KAIST), Daejeon 34141, Korea

⁴ These authors contributed equally: Jin-Oh Kim, Won-Tae Koo.

Corresponding authors: I.-D.K (idkim@kaist.ac.kr), S.P. (stevepark@kaist.ac.kr)

Keywords: Conductive metal-organic frameworks, Microfluidic, Solution shearing, Gas sensors.

Abstract

Conductive metal-organic framework (C-MOF) thin-films have a wide variety of potential applications in the field of electronics, sensors, and energy devices. The immobilization of various functional species within the pores of C-MOFs can further improve the performance and extend the potential applications of C-MOFs thin-films. However, there are currently no effective strategies for facile and scalable synthesis of high quality ultra-thin C-MOFs while simultaneously immobilizing functional species within the MOF pores. Here, we develop microfluidic channel-embedded solution-shearing (MiCS) for ultra-fast (≤ 5 mm/s) and large-area synthesis of high-quality nanocatalyst-embedded C-MOF thin-films with thickness controllability down to tens of nanometers. The MiCS method synthesizes nanoscopic catalyst-embedded C-MOF particles within the microfluidic channels, and simultaneously grows catalyst-embedded C-MOF thin-film uniformly over a large area using solution shearing. The thin-film displays highest nitrogen dioxide (NO₂) sensing properties at room temperature in air amongst two-dimensional materials, owing to the high surface area and porosity of the ultra-thin C-MOFs, and the catalytic activity of the nanoscopic catalysts embedded in the C-MOFs. Therefore, our method, *i.e.* MiCS, can open new avenues of highly active and conductive porous materials for various applications.

Conductive metal organic frameworks (C-MOFs) are a new class of materials receiving a great deal of interest in recent years due to their many attractive properties such as high porosity, narrow pore-size distribution and periodically organized pores, adjustable band gap, and designable electrical charge transport properties^{1, 2, 3, 4, 5}. These properties broadened the applicability of metal organic frameworks (MOFs) (which have traditionally been electrically insulating) to novel applications such as transistors⁶, electrodes^{7, 8, 9, 10}, and resistive chemical sensors^{11, 12, 13, 14}.

The key features of MOFs are their high porosity and regularly arranged pores. These pores can be utilized to immobilize nanoscale catalyst such as Au, Pd, and Pt, and since the reactivity of the catalysts improves with increasing surface area, well-dispersed nanoscale catalysts can drastically enhance the overall catalytic performance of MOFs^{15, 16, 17, 18, 19}. Recently, the immobilization of nanocatalyst has been applied to C-MOFs, and was demonstrated of enhancing the performance of Li-S batteries²⁰ and gas sensors¹⁵.

The C-MOF applications mentioned above require the formation of high quality thin-films with controlled film thickness down to nanometer scale (less than 100 nm), smooth and uniform surface, and densely-packed thin-film MOF particles to ensure fast transport of charge carriers across the thin-film²¹. Furthermore, immobilization of nanocatalyst into the pores is needed to optimize the catalytic performance of C-MOF thin-films. Currently, the main techniques to generate nanoscale thin-films of C-MOFs are layer-by-layer^{14, 22}, and interfacial synthesis^{6, 23, 24}. Although high quality C-MOF films can be generated with these techniques, simultaneous immobilization of nanocatalyst during C-MOF thin-film synthesis is difficult. In general, embedding of nanocatalyst within MOF films has been done by firstly synthesizing MOF crystals in the bulk, and subsequently exposing it to metal precursor solution, followed by reduction reaction. The nanocatalyst-embedded MOF crystals are then deposited as a thin-film^{11, 12, 25}. However, this technique inevitably requires multiple relatively slow processes, and

results in poor thin-film quality. To the best of our knowledge, there is currently no technique to generate high quality nanoscale C-MOF thin-film with embedded nanocatalyst particles within the pores.

Herein we introduce microfluidic channel-embedded solution-shearing (MiCS) as a means to immobilize metal nanoparticles (*i.e.* nanocatalysts) into the C-MOFs pores during thin-film synthesis, through which high quality nanocatalyst-embedded C-MOF thin-films were generated with thickness control down to tens of nanometers. Furthermore, contrary to other MOF thin-film growth techniques^{14, 22}, MiCS can generate MOF thin-film over a large-area in a scalable and high-throughput (5 mm/s) manner, rendering it a feasible technique for large-scale manufacturing. Solution shearing is a technique analogous to blade coating, where a fixed amount of solution is sandwiched between a moving blade and a heated substrate^{26, 27, 28}. A meniscus (curved air-liquid interface) naturally forms between the blade and the substrate, and as the meniscus moves along with the moving blade, thin-film is deposited across the substrate as solution-to-solid transition occurs near the edge of the meniscus.²⁶ **Fig. 1a** is a schematic depiction of metal nanoparticle-embedded C-MOF thin-film formation using MiCS. Contrary to conventional solution shearing, in MiCS, microfluidic channels have been embedded within the blade, and these channels act as microreactors for chemical synthesis of nanocatalyst-embedded C-MOFs. **Fig. 1b** is the depiction of the microfluidic channel design. Cu metal precursor solution and organic ligand (2,3,6,7,10,11-hexahydroxytriphenylene [HHTP])/reducing agent (NaBH₄) solution was firstly mixed together, inducing nucleation of Cu₃(HHTP)₂ C-MOF particles. This solution was then mixed with Pt precursor solution, which immobilizes the Pt nanocatalyst particles within the C-MOF pores. As the solution containing the Pt-embedded Cu₃(HHTP)₂ C-MOF (Pt@Cu₃(HHTP)₂) particles flow out onto the heated substrate (150 °C), particles grow into a thin-film on the substrate, as depicted in **Fig. 1c** and **1d**. Therefore, MiCS is a unique technique where the reduction of nanocatalyst, synthesis of

nanocatalyst-embedded C-MOFs, and the growth of thin-film occurs concurrently all in a single step. **Supplementary Table 1** summarizes the pros and cons to various MOF thin-film formation techniques. In order for MiCS to work properly, the synthesis of $\text{Pt@Cu}_3(\text{HHTP})_2$ particles must occur on the same time scale as that of the solution shearing rate. In this regard, the use of microfluidic reactors enable extremely fast mixing and mass transfer effects unachievable by batch systems, leading to significantly enhanced reaction rates^{29, 30, 31}. Hence, despite the short reaction time, continuous synthesis of $\text{Pt@Cu}_3(\text{HHTP})_2$ particles during solution shearing is possible. Furthermore, the fast reaction rate and precisely controlled reaction time yield uniformly sized Pt nanoparticles and $\text{Cu}_3(\text{HHTP})_2$ particles.

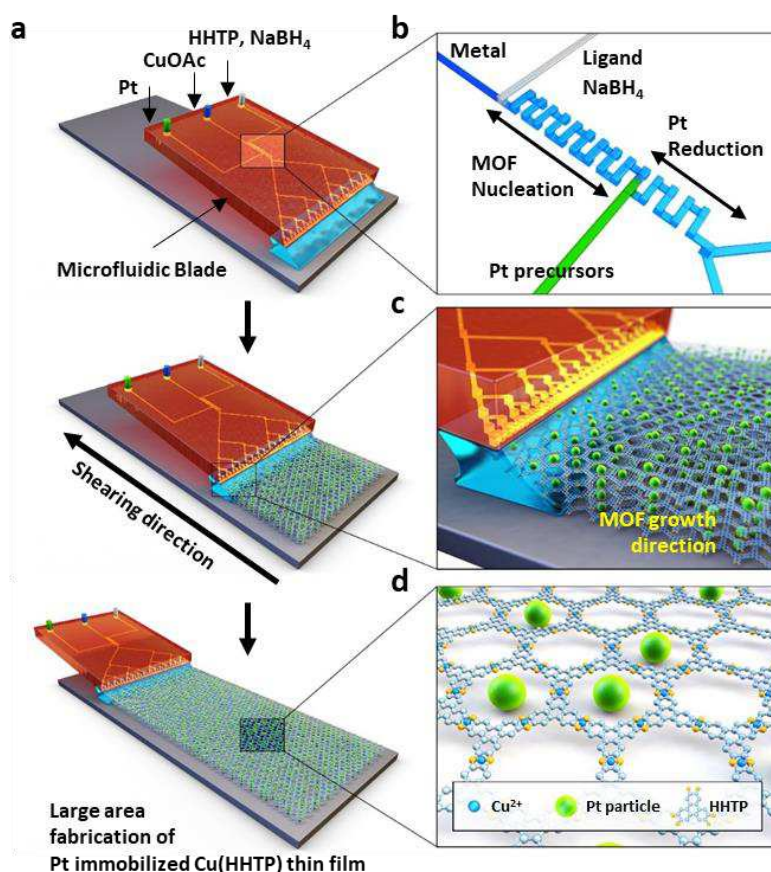


Fig. 1: Fabrication of $\text{Pt@Cu}_3(\text{HHTP})_2$ thin-film using MiCS. **a**, Schematic of $\text{Pt@Cu}_3(\text{HHTP})_2$ MOF thin-film processing using microfluidic-based solution shearing process. CuOAc is copper(II) acetate. **b**, Schematic illustration of the microfluidic blade channel **c**, Schematic illustration of the MOF growth process using solution shearing. The nucleated Pt-particle embedded MOF solution is located between the microfluidic blade and

the heated substrate. The MOF growth occurs at the edge of the meniscus. With the continuously supplying solution by the microfluidic blade during solution shearing, large-area and uniform Pt@Cu₃(HHTP)₂ thin-film can be formed. **d**, Crystal structure of Pt@Cu₃(HHTP)₂ thin-film (green sphere: Pt particle). @ means –embedded.

Fig. 2a is an optical image of the microfluidic channel-embedded solution shearing blade; further details regarding the microfluidic chip design is described in **Supplementary Fig. 1**. The microfluidic channels were designed as a three-dimensional serpentine mixer (**Supplementary Fig. 2**) due to its high mixing efficiency³². **Fig. 2b** are top view optical images of the microfluidic channels at various cycling points, and **Fig. 2c** and **2d** are the corresponding computational fluid dynamics (CFD) simulation results depicting the degree of mixing. As the number of cycles increase, the degree of mixing increases, as indicated by the appearance of the light green colored solution. The flow rate was optimized using CFD simulation, where various flow rates were evaluated by monitoring the degree of mixing as a function of number of cycles (**Supplementary Tables 2-5**). When the flow rate exceeded 220 $\mu\text{L}/\text{min}$, 15 mixing cycles were sufficient to fully mix the solutions, as seen in **Fig. 2e**. At this flow rate, the solution residence time within the microfluidic channel is short (200 ms, **Supplementary Fig. 3**), which prevented the microfluidic channels from being clogged due to particle aggregation.

Fig. 2f are optical images of the Pt@Cu₃(HHTP)₂ thin-film using conventional solution shearing (left), and MiCS (right). In the case of solution shearing, all of the components were premixed as a bulk solution, and the solution was inserted in between the blade and the substrate prior to coating. Over a large area, the thin-film coated with MiCS exhibited high degree of uniformity without the presence of particle aggregates. This was on the contrary to thin-film coated with conventional solution shearing, which visually showed variability in film color and particle aggregates. The surface roughness of the film made with MiCS was 2.8 nm; whereas, that of the solution shearing was 92.3 nm (**Supplementary Fig. 4**). Such thin-film properties attained using MiCS can be attributed to the controlled nucleation

reaction of the precursor solution within the microfluidic channel, and the continuous supply of solution that maintains constant solution volume, concentration, and the shape of the meniscus during coating. These factors can alter the fluid behavior near the meniscus, which can change the thin-film properties³³. **Fig. 2g** and **2h** are scanning electronic microscopy (SEM) images of the Pt@Cu₃(HHTP)₂ thin-film fabricated using MiCS, confirming the closely-packed MOF thin-film without pinholes. Powder x-ray diffraction (PXRD) was conducted on Pt@Cu₃(HHTP)₂ thin-film grown on the substrate and on the nucleated Pt@Cu₃(HHTP)₂ particles being extruded out of the microfluidic channels (without undergoing thin-film growth on the substrate) (**Supplementary Fig. 5**). Much weaker diffraction peaks were observed for the latter case, which confirm that Pt@Cu₃(HHTP)₂ thin-film is grown on the substrate after being extruded out of the microfluidic channels. Previous C-MOF growth techniques indicate that elevated temperature is needed for thin-film growth since energy is required to form coordination bonds; this corroborates the XRD results³⁴. As stated above, the simultaneous synthesis and growth of thin-film is a unique feature of MiCS, which allows the formation of densely packed high-quality film with low surface roughness and nanoscale thickness control (discussed below).

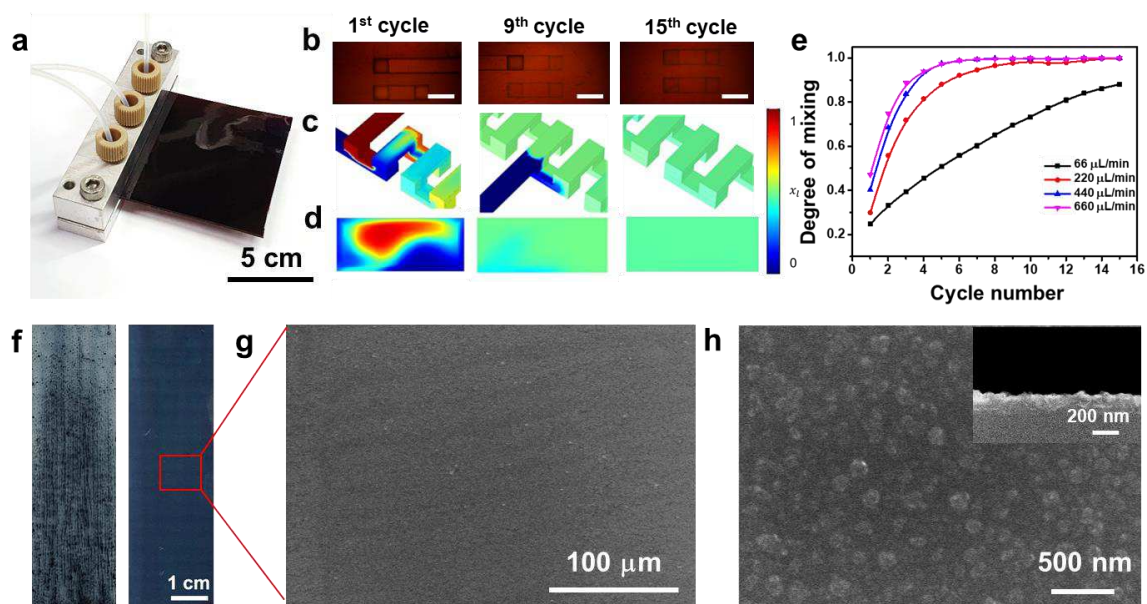


Fig. 2: Characterization of MiCS. **a**, Photographic image of the polyimide microfluidic blade. **b**, Optical image of polyimide microfluidic device channel (Scale bar: 500 μm): 1st cycle (left), 9th cycles (middle), 15th cycles (right). **c**, 3D surface and **d**, 2D cross sectional concentration distribution of solution (x_l) at 1st (left), 9th (middle), and 15th (right) cycle under 660 $\mu\text{l}/\text{min}$ flow rate. **e**, Effect of cycle number on the degree of mixing obtained at various flow rates. **f**, Optical image of solution sheared Pt@Cu₃(HHTP)₂ film: without microfluidic blade (left), and with microfluidic blade (right). **g**, SEM image of Pt@Cu₃(HHTP)₂ thin-film. **h**, High resolution SEM image of Pt@Cu₃(HHTP)₂ thin-film. @ means –embedded.

To confirm the immobilization of Pt nanoparticle within the MOF pores, cryo-transmission electronic microscopy (Cryo-TEM) was used to attain (001) plane view images of Pt@Cu₃(HHTP)₂, as depicted in Fig. 3a-c. Fig. 3b and 3c are close-up of the MOF pores in the region absent of and immobilized with Pt particles, respectively, showing a clear difference in the image contrast. Fig. 3d plots the integrated pixel intensities for the empty Cu₃(HHTP)₂ and Pt immobilized Cu₃(HHTP)₂ unit cells along the [100] direction. The [100] lattice spacing (d_{100}) for the empty Cu₃(HHTP)₂ across 5 unit cells was measured to be *c.a.* 2.0 nm, which is in good agreement with the theoretical pore size of Cu₃(HHTP)₂²². In the case of Pt@Cu₃(HHTP)₂, since the beam cannot pass through the Pt particles, darker regions within the pores were observed. To further identify the Pt particles, high-resolution-TEM (HRTEM) was used to damage the MOF structure and observe the Pt particles, as depicted in

Supplementary Fig. 6. As shown in **Supplementary Fig. 6a**, Pt particles having an average diameter of 2 nm are well dispersed in $\text{Cu}_3(\text{HHTP})_2$. **Supplementary Fig. 6b** show the lattice of the Pt (111) plane with a spacing of 2.265 Å. Scanning TEM (STEM) image of $\text{Pt@Cu}_3(\text{HHTP})_2$ demonstrated that the Pt particles are well dispersed throughout the $\text{Cu}_3(\text{HHTP})_2$ structure (**Supplementary Fig. 6c**). The presence of Cu, C, O and Pt elements in the sample was confirmed by TEM-EDS element mapping (**Supplementary Fig. 6d**). Comparing the HR-TEM images of $\text{Pt@Cu}_3(\text{HHTP})_2$ made using conventional bulk synthesis technique¹⁵ to that of MiCS (**Supplementary Fig. 7**) showed that the size variance of the Pt particles was much higher for the former. This can be attributed to the rapid and controlled Pt reduction reaction within the microfluidic channels³⁵.

The thickness of $\text{Pt@Cu}_3(\text{HHTP})_2$ thin-film can be precisely controlled at tens of nanometer level using MiCS (**Fig. 3e**). The film thickness at various shearing speeds was confirmed using atomic force microscopy (AFM) images (**Supplementary Fig. 8**). The thickness decreasing with increasing shearing speed indicates that the system is in evaporative regime, where the solvent evaporation rate is on a similar time scale to the shearing rate³⁶. In this regime, thickness variation can theoretically be explained by the mass balance between the evaporating solvent and the depositing thin-film to the solution flowing towards the meniscus,³⁶ with a power law, thickness \propto speed⁻¹. Our data indicates a power dependence of -0.99, which is in good agreement with the theoretical value. Ultraviolet–visible (UV/Vis) spectra were taken on $\text{Pt@Cu}_3(\text{HHTP})_2$ films of various thickness, as seen in **Fig. 3f**. The characteristic absorbance at 363 nm (π - π^* transition) and 645 nm (ligand to metal charge transfer band) increased with decreasing the shearing speed due to the increasing film thickness^{14, 22}. The crystal structures of $\text{Cu}_3(\text{HHTP})_2$ and $\text{Pt@Cu}_3(\text{HHTP})_2$ were investigated by powder X-ray diffraction (PXRD) analysis (**Fig. 3g**). The pristine $\text{Cu}_3(\text{HHTP})_2$ showed the crystal planes of (100), (200), (001), (220), and (112), which was similar to observation in previous literature¹⁰,

²⁵. Pt@Cu₃(HHTP)₂ showed the same diffraction pattern as pristine Cu₃(HHTP)₂ without a clear appearance of Pt diffraction peak (at 2θ = 42°). This can be attributed to the very small amount of Pt particles and their embedment into the MOF pores¹⁹. The N₂ adsorption and desorption isotherms at 77K confirmed the porous nature of Cu₃(HHTP)₂ and Pt@Cu₃(HHTP)₂ (Supplementary Fig. 9). The Brunauer–Emmett–Teller (BET) surface area of Pt@Cu₃(HHTP)₂ was 200 m² g⁻¹, which showed a decreased value than the surface area of Cu₃(HHTP)₂ (250 m² g⁻¹). This can be ascribed to the Pt particles blocking the MOF pores¹¹.

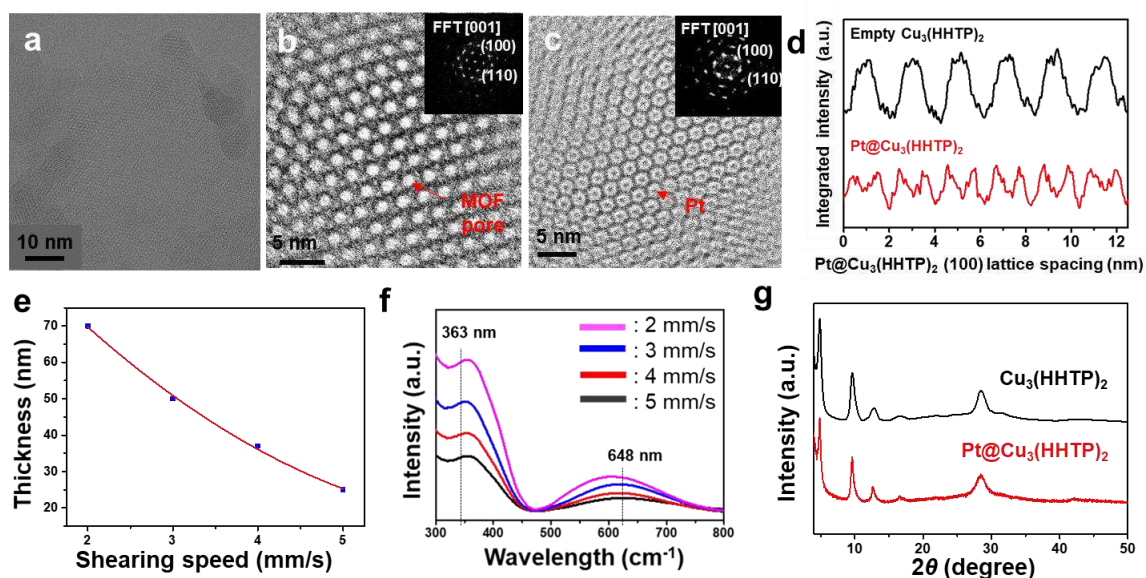


Fig. 3: Characterization of Pt@C-MOF thin-films fabricated by MiCS. **a-c**, Cryo-TEM images of Pt@Cu₃(HHTP)₂: **b**, without Pt particle in the MOF pores. **c**, Pt particle immobilized in the MOF pores. **d**, Integrated intensity of Pt@Cu₃(HHTP)₂ plotted over 6 unit cells along the [100] direction, indicating a pattern when Pt particle is introduced into the pores. **e**, Thickness control of Pt@Cu₃(HHTP)₂ thin-film via controlling the shearing speeds. **f**, UV-Vis spectrum of different thicknesses of Pt@Cu₃(HHTP)₂ thin-film. **g**, PXRD data of Cu₃(HHTP)₂ and Pt@Cu₃(HHTP)₂. @ means –embedded.

To demonstrate the ultra-high catalytic activity and potential applications of Pt@Cu₃(HHTP)₂ thin-film, we investigated its chemiresistive sensing properties. Chemiresistors are in high demand for a wide range of applications, such as environmental monitoring³⁷, exhaled breath analysis³⁸, and food quality control³⁹. However, there are grand challenges in chemiresistive sensors: low responses to sub-ppm levels of analytes, poor cross-

selectivity, and high power consumption. We postulated that our thin-films can address these issues because they have high surface area and porosity, ultra-high reactivity, and can be operated at room temperature. In addition, since MiCS-based thin-film has uniform electrical characteristics (see **Supplementary Fig. 10** for comparison between MiCS-based and conventional solution shearing-based thin-film electrical properties), a relatively reliable sensing data can be attained. We fabricated chemiresistors using Pt@Cu₃(HHTP)₂ thin-film along with control samples (Cu₃(HHTP)₂ powder and pristine Cu₃(HHTP)₂ thin-film) (see details in the Methods). Firstly, to optimize the NO₂ sensing properties of Pt@Cu₃(HHTP)₂ thin-film-based sensors at room temperature in air, we controlled the loading amounts of Pt nanoparticles by the different flow rate of Pt precursors (50, 100, 150, and 200 μL/min) (**Supplementary Fig. 11**). The weight ratio of Pt-loaded Cu₃(HHTP)₂ were calculated using Inductively Coupled Plasma Mass Spectrometer analysis (ICP-MS) (**Supplementary Table 6**). Among the samples, the 2.3 wt% Pt-loaded Cu₃(HHTP)₂ thin-film exhibited the optimum NO₂ sensing properties (hereafter, the 2.3 wt% Pt-loaded Cu₃(HHTP)₂ thin-film represents the Pt@Cu₃(HHTP)₂ thin-film-based NO₂ sensors).

The Pt@Cu₃(HHTP)₂ thin-film displays significant resistance changes ($\Delta R/R_a = -89.9\%$) at 3 ppm of NO₂ (**Fig. 4a**). In contrast, the Cu₃(HHTP)₂ powder and Cu₃(HHTP)₂ thin-film show lower responses (-11.8% for Cu₃(HHTP)₂ powder and -53.7% for Cu₃(HHTP)₂ thin-film) relative to the Pt@Cu₃(HHTP)₂ thin-film. In addition, the Pt@Cu₃(HHTP)₂ and Cu₃(HHTP)₂ thin-films are able to detect NO₂ as low as 0.1 ppm, whereas the Cu₃(HHTP)₂ powder do not function below 1 ppm (**Supplementary Fig. 12**). We calculated normalized responses ($|\Delta R/R_0|$) and response times (t_{90}) of the sensors in the range of NO₂ 0.1–3 ppm (**Fig. 4b** and **Supplementary Fig. 13**). The formation of thin-film structure (Cu₃(HHTP)₂ thin-film) improves the responses of Cu₃(HHTP)₂ by a factor of 4, compared to Cu₃(HHTP)₂ powder. In addition to the structural effect, the decoration of Pt nanoparticles (Pt@Cu₃(HHTP)₂ thin-film)

induces 2-fold higher responses than pristine $\text{Cu}_3(\text{HHTP})_2$ thin-film. Furthermore, the $\text{Pt}@Cu_3(\text{HHTP})_2$ thin-film shows faster sensing speed (8.2 min to NO_2 3 ppm) compared to the $\text{Cu}_3(\text{HHTP})_2$ thin-film (14 min) and $\text{Cu}_3(\text{HHTP})_2$ powder (17.3 min). These results demonstrated that both thin-film structure of $\text{Cu}_3(\text{HHTP})_2$ and ultra-small Pt nanoparticles increase the activity of the sensors. Although the response times of the $\text{Pt}@Cu_3(\text{HHTP})_2$ thin-film are sluggish at low NO_2 concentrations (< 1 ppm), the $\text{Pt}@Cu_3(\text{HHTP})_2$ thin-film-based sensors (13 min for NO_2 1 ppm) meet the safety standard for NO_2 exposures; the short-term permissible exposure limit of NO_2 , designated by the Occupational Safety and Health Administration (OSHA) in the United States, is 1 ppm within 15 min.

We further investigated the other important parameters for NO_2 sensors: selectivity and stability. The $\text{Pt}@Cu_3(\text{HHTP})_2$ thin-film sensors display ultra-high NO_2 cross-selectivity against other interfering analytes (hydrogen sulfide [H_2S], acetone [CH_3COCH_3], ethanol [$\text{C}_2\text{H}_5\text{OH}$], methanethiol [CH_3SH], toluene [$\text{C}_6\text{H}_5\text{CH}_3$], and carbon monoxide [CO]) (**Fig. 4c**). The responses (55.3%) of the $\text{Pt}@Cu_3(\text{HHTP})_2$ thin-film to NO_2 are 10-fold higher than those ($> 5.2\%$) to other gas molecules. In addition, the sensors show stable responses to multiple exposures to NO_2 0.1 ppm (**Supplementary Fig. 14a**), demonstrating high feasibility as dosimetric sensors. Furthermore, the $\text{Pt}@Cu_3(\text{HHTP})_2$ thin-film-based sensors function well in humid air (relative humidity = 95%) (**Supplementary Fig. 14b**). There are slight decreases in the response (-38.9% to NO_2 1 ppm) and response speed (18 min) under the humid air (relative humidity: 90%) compared to those (response = -55.3% and response time = 13 min) under the dry air (relative humidity: 5%). These decreases are attributed to the fact that adsorbed water molecules retard the reactions of NO_2 on $\text{Pt}@Cu_3\text{HHTP}_2$ thin-film. Nonetheless, these sensing performances demonstrate that our sensors represent a viable NO_2 sensor operated at room temperature in air.

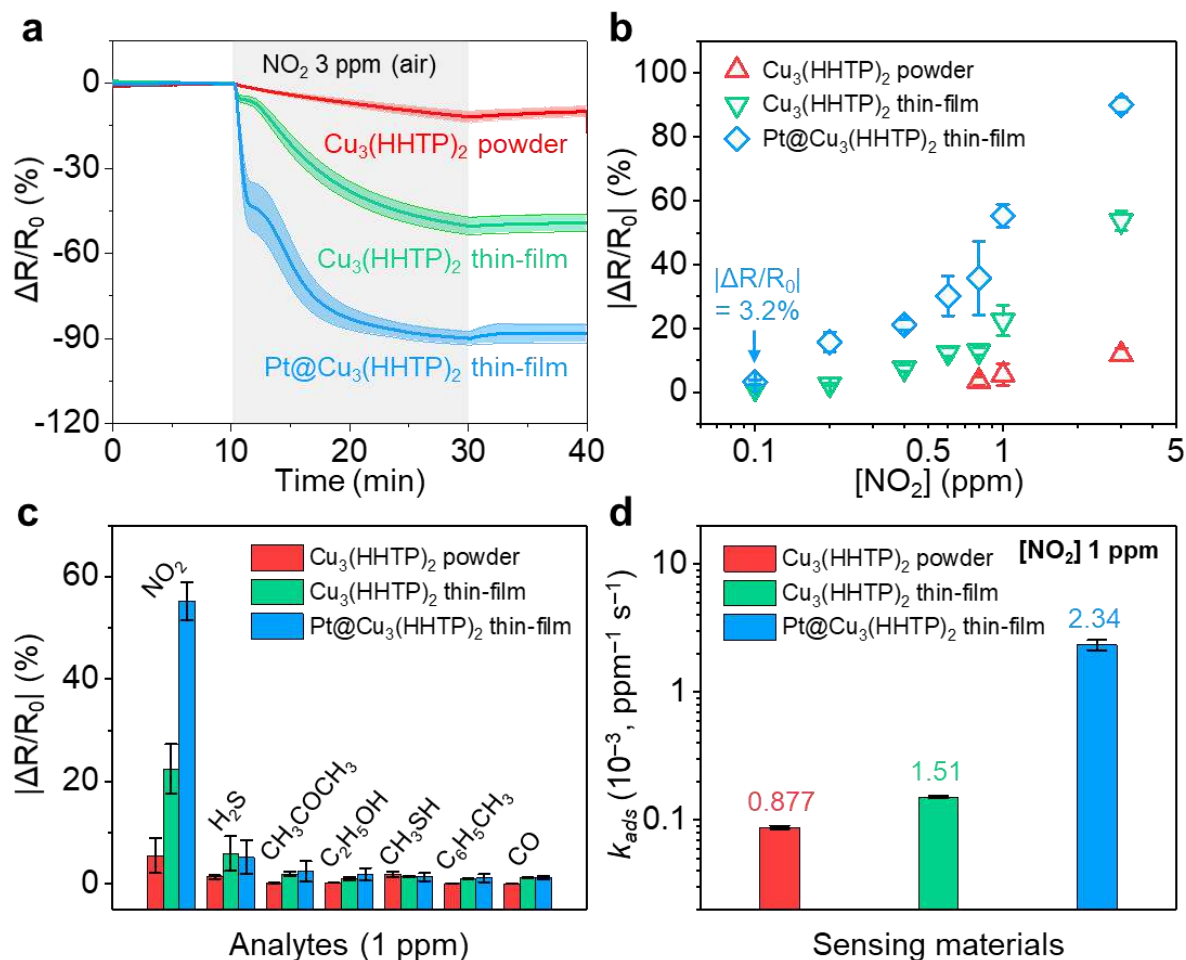


Fig. 4: Sensing characteristics of Pt@Cu₃(HHTP)₂ thin-film. **a**, Resistance changes of Cu₃(HHTP)₂ powder, Cu₃(HHTP)₂ thin-film, and Pt@Cu₃(HHTP)₂ thin-film in response to 20 min exposure of NO₂ 3 ppm. The shaded areas present the standard deviation of the sensors ($N \geq 4$). **b**, Normalized responses of the sensors to 0.1–3 ppm of NO₂. **c**, Selectivity of the sensors to 1 ppm of analytes. **d**, Calculated adsorption rate constants (k_{ads}) of the sensors. @ means – embedded.

To elucidate the structural and catalytic effect of Pt@Cu₃(HHTP)₂ thin-film on NO₂ sensing, we calculated adsorption rate kinetics (k_{ads}) using response traces of the sensors. Since the origin of chemiresistive sensing of Cu₃(HHTP)₂ is charge transfers caused by adsorbed gas molecules^{12, 40}, with the assumption that the responses of Cu₃(HHTP)₂ are proportional to the amounts of adsorbed NO₂ molecules, reaction rate constants are obtained by fitting responses traces to theoretical equations (see details in **Supplementary Fig. 15** and **Supplementary**

Table 7). The calculated k_{ads} values are described in **Fig. 4d**. The Pt@Cu₃(HHTP)₂ thin-film shows higher NO₂ adsorption kinetics ($k_{ads} = 2.34 \times 10^{-3} \text{ ppm}^{-1} \text{ s}^{-1}$) than the Cu₃(HHTP)₂ powder ($0.877 \times 10^{-3} \text{ ppm}^{-1} \text{ s}^{-1}$) and the Cu₃(HHTP)₂ thin-film ($1.51 \times 10^{-3} \text{ ppm}^{-1} \text{ s}^{-1}$), demonstrating that NO₂ reactions on Cu₃(HHTP)₂ are promoted by two factors: (1) the thin-film structure of Cu₃(HHTP)₂ and (2) the catalytic effect of ultra-small Pt NPs. The thin-film structure induces high gas accessibility into sensing layers¹⁴, and ultra-small Pt NPs (~2 nm) cause NO₂ spillover onto Cu₃(HHTP)₂¹⁵. Therefore, NO₂ molecules are easily accessible to Cu₃(HHTP)₂ layers and their reactions are activated by nanoscopic Pt catalysts, leading to the exceptionally high sensing performances. These outstanding sensing performances outperform the current state-of-the-art 2D material-based NO₂ chemiresistors operated at room temperature in air (**Fig. 5** and **Supplementary Table 8**)^{15, 41, 42, 43, 44, 45, 46, 47, 48, 49, 50}. To the best of our knowledge, the NO₂ responses of our sensors are the highest among MOF-based NO₂ sensors, and even superior to other 2D materials, including graphene, transition metal dichalcogenides (TMDs), and their composites.

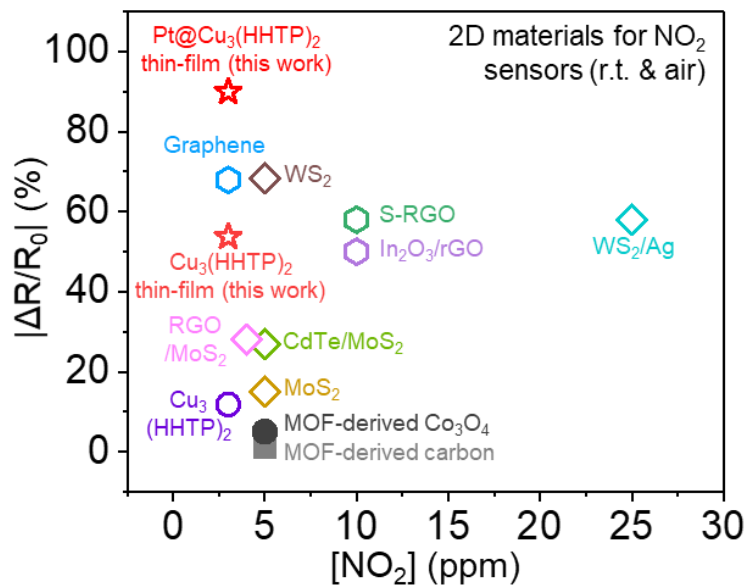


Fig. 5: Comparison of the NO₂ responses of Pt@Cu₃(HHTP)₂ thin-film and Cu₃(HHTP)₂ thin-film with those of other materials. Other materials include Cu₃(HHTP)₂, graphene, WS₂,

RGO/MoS₂ (RGO: reduced graphene oxide), CdTe/MoS₂, MoS₂, MOF-derived CO₃O₄, MOF-derived carbon, S-RGO (S-RGO: sulfonated RGO), In₂O₃/RGO, and WS₂/Ag.

Conclusion

C-MOFs are a new class of materials with high degree of chemical versatility and ultra-high porosity, rendering them a suitable material for next-generation electronics, energy storage devices, and sensors. To fully take the advantage C-MOFs, generation of high-quality nanoscale thin-films with the versatility to immobilize nanocatalysts into the MOF pores is of critical importance. This has thus far been a major challenge as simultaneous synthesis of MOF thin-film and immobilization of nanocatalysts has not been possible. Furthermore, high-throughput, large-area, single-step (synthesis, film growth, catalyst immobilization) thin-film generation has not been demonstrated, limiting the commercial feasibility of C-MOFs. Our proposed MiCS technique overcomes these difficult challenges. The use of microfluidic channels enable synthesis of catalyst-embedded MOF particles, which simultaneously grows into high-quality nanoscale thin-film in a large-area scalable, high-throughput manner. Our thin-films exhibit the highest gas sensing performance to date, as a consequence of (1) the high porosity and facile gas accessibility of C-MOF thin-films, and (2) the ultra-high catalytic activity of the embedded nanoparticles (*c.a.* 2 nm). These results together points to the exciting prospects of utilizing MiCS for the generation and optimization of a variety of catalyst-embedded C-MOF thin-films for various applications in the future.

Methods

Materials. All chemicals and solvents were of reagent grade and were used as received without further purification. Copper(II) acetate monohydrate (Cu(CO₂CH₃)H₂O, 99.9 %), dimethyl sulfoxide (DMSO), Potassium tetrachloroplatinate(II) (K₂PtCl₄), and sodium borohydride (NaBH₄, 96%) were purchased from Sigma-Aldrich. 2,3,6,7,10,11-hexahydroxytriphenylene

hydrate (HHTP, $C_{18}H_{12}O_6H_2O$, 95.0%) was purchased from Tokyo Chemical Industry.

Mathematical formulation and numerical details. The flow behavior and mixing progress in the microfluidic mixing region were investigated numerically based on the finite element method (FEM) with *COMSOL Multiphysics software* (v5.5, Comsol Inc.). The computation of steady-state fluid flow was followed by the mass transfer analysis based on the derived velocity profile.

The flow regime ($Re \sim \mathcal{O}(10) \ll 2,000$) for present work was considered as laminar flow, so the turbulent model was not involved³². The velocity (v) and pressure (p) profile were derived by numerically solving the governing equations as below:

$$\rho(v \cdot \nabla)v = -\nabla \cdot [-pI + K] \quad : \text{Navier-Stokes equation,}$$

$$\nabla \cdot v = 0 \quad : \text{Continuity equation,}$$

$$K = \mu(\nabla v + (\nabla v)^T) \quad : \text{Constitutive equation,}$$

where the density (ρ) and viscosity (μ) followed the solvent's properties, dimethyl sulfoxide (DMSO, whose $\rho = 1.1 \text{ g/mL}$ and $\mu = 2 \text{ mPa} \cdot \text{s}$). Concentration dependence on viscosity and density could be neglected based on the comparison of calculation results under similar conditions in previous work³². As boundary conditions, the mass flow rate for inlet, non-slip condition on the inner surface of the wall, and ambient air pressure on the outlet were applied.

The concentration change of NaBH_4 ligand (C_l), CuOAc metal (C_m), and Pt precursors (C_{Pt}) in DMSO were derived by solving governing equations for mass transfer as below:

$$\nabla \cdot J_i + v \cdot \nabla c_i = R_i \quad : \text{Mass conservation equation,}$$

$$J_i = -D\nabla c_i \quad : \text{Fick's diffusion equation,}$$

where the generic molecular diffusivity ($10^{-9} \text{ m}^2/\text{s}$) were applied for the molecular diffusivity (D). Because the Péclet number for the present study is in the range of $10^3 \leq Pe \leq 2 \times 10^4$, convection-mediated mass transfer dominates mass transfer. Nucleation and catalyst embedding are sufficiently fast to assume that the degree of mixing directly indicates the conversion of HHTP nucleation and Pt reduction. In other words, under steady-state condition, right-hand side of the mass conservation equation was considered zero. For the boundary

condition of mass transfer, the individual initial concentrations for each inlet and no mass flux gradient for outlet were applied.

The geometry exactly the same as the microfluidic blade was manually constructed and was divided into computational elements in COMSOL, where the number of elements was determined by the mesh size dependency test. To achieve adequate calculation accuracy within the limits allowed by computational power (2.1 GHz 24 core CPU, 250 GB RAM), first, second, and quadratic order discretization was applied for pressure, velocity, and concentration, individually.

Microfluidic cycle and degree of mixing (ε). For indication and evaluation, the entire microfluidic blade was divided into microfluidic cycles as defined in **Supplementary Fig. 2**. Except for the 1st cycle, each cycle includes 4 turns and experiences the same residence time determined by the mass flow rate. The plane between the n^{th} cycle and $n+1^{\text{th}}$ cycle is defined as P_{n+1} ($n \geq 1$), and P_1 is considered as the plane where the ligand and metal first meet, so the first cycle has only 2 turns after P_1 .

The degree mixing was calculated at each plane (P_n) showing the result of each n^{th} cycle. From the numerical solution of each solutes' concentration, the molar fraction of ligand ($x_l = \frac{c_l}{\sum_i c_i}$, $i = l, m, \text{ and } Pt$) is used in order to quantify the degree of mixing which directly denotes the progress of MOF nucleation and Pt reduction. The degree of mixing (ε) is defined with its standard deviation of x_l (σ), as below:

$$\varepsilon = 1 - \frac{\sigma}{\sigma_{max}} \quad : \text{Degree of mixing.}$$

The maximum standard deviation (σ_{max}) was designated at the plane where the ligand or Pt precursor and metal meet first (i.e., $\sigma_{max} = 0.498$ for ligand-metal and 0.287 for ligand-Pt precursor at P_1).

Fabrication of microfluidic blade. The microfluidic-channel embedded blade was made using a method previously reported³². Firstly, PI films of 125 μm in thickness (Kapton HN film, Dupont, USA) were ablated using UV laser (355 nm, ESI, USA) to form the desired micro patterns (300 μm in width). In laser ablated regions were completely eliminated of the PI films. Thereafter, FEP (fluoroethylene propylene) nano powder dispersed in aqueous solution was

spin-coated (2000 rpm, 50s) onto each of the PI films. Then the FEP coated PI films were vertically stacked using a metal holder with aligners. Finally, the aligned PI films were mechanically pressed at 350 °C under a pressure of 10 kPa for 3 hrs.

Synthesis of $\text{Cu}_3(\text{HHTP})_2$ film using MiCS process. A solution of Copper(II) acetate monohydrate (0.12 M in DMSO, 200 $\mu\text{L}/\text{min}$) and a solution of HHTP (0.1 M in DMSO, 200 $\mu\text{L}/\text{min}$) were introduced into two inlets of the microfluidic blade continuously using syringe pumps (Harvard Apparatus PHD 4400) at a rate of 400 $\mu\text{L}/\text{min}$. The microfluidic channels were shaped as 3-dimensional serpentine structure with a total of 15 cycles of mixing to induce effective mixing. The reacted solution discharged through the 64-outlets of microfluidic blade onto to heated substrate. The gap (i.e., distance between microfluidic blade and substrate) and angle were set at 100 μm and 30°, respectively. The generated $\text{Cu}_3(\text{HHTP})_2$ thin-film was washed with DMSO and ethanol, respectively.

Synthesis of $\text{Pt}@\text{Cu}_3(\text{HHTP})_2$ film using MiCS process: A solution of copper(II) acetate monohydrate (0.12 M in DMSO, 200 $\mu\text{L}/\text{min}$) and a mixed solution of HHTP with NaBH_4 (HHTP: 0.1 M in DMSO, NaBH_4 : 1 mg mL^{-1} , 200 $\mu\text{L}/\text{min}$) were introduced to two inlets of the microfluidic blade using syringe pumps. Pt solution (1 mg mL^{-1} , 50, 100, 150, and 200 $\mu\text{L}/\text{min}$) was inserted at the 9th cycle of mixing. The resulting solution discharged continuously between the microfluidic blade and heated substrate. The gap (i.e., distance between microfluidic blade and substrate) and angle were set at 100 μm and 30°, respectively. The generated $\text{Pt}@\text{Cu}_3(\text{HHTP})_2$ thin-film was washed with DMSO and ethanol, respectively.

Material characterization: Cryo Field Emission TEM (Glacios, Thermo Fishter) at 200 kV, Field-emission TEM (Tecnai G2 S-Twin, FEI) at 300 kV and spherical aberration-corrected TEM (JEMARM200F, JEOL) at 200 kV were conducted to investigate the microstructure of the samples. The MOF thin-films were imaged using a field emission scanning electron

microscope (FE-SEM, Hitachi S-4800). X-ray diffraction (XRD) patterns were measured by D/Max-2500 (RIGAKU) diffractometer. Film thickness and topology were measured with tapping mode AFM (AFM WORKSHOP, PS-2010). The nitrogen adsorption-desorption isotherms were obtained using a BELSORP-max at 77 K. Prior to the adsorption measurements, all samples (~100 mg) were evacuated ($p < 10^{-5}$ mbar) at 393 K for 5 h. The specific surface area was obtained by the Brunauer-Emmett-Teller (BET) method.

Sensing measurements. $\text{Cu}_3(\text{HHTP})_2$ and $\text{Pt}@\text{Cu}_3(\text{HHTP})_2$ thin-films were directly formed on alumina (Al_2O_3) substrate (2.5 mm [width] \times 2.5 mm [length] \times 0.2 mm [thickness]). Bulk $\text{Cu}_3(\text{HHTP})_2$ based sensors were prepared by drop-coating suspension of the $\text{Cu}_3(\text{HHTP})_2$ powder (5 mg in 300 μL of ethanol) onto the alumina substrate. To trace the resistance of the sensors, Au electrodes with a gap of 70 μm were deposited on top of the films. NO_2 sensing tests were carried out at room temperature in air. Before the sensing tests, the sensors were stabilized by fresh air for 4 h. Thereafter, the sensors were exposed to NO_2 for 20 min, with the NO_2 concentrations controlled in the range of 0.1–3 ppm using mass flow controller. Resistance of the sensors were monitored using an acquisition system (34972, Agilent) in real time. Response was defined as a ratio of the resistance change (ΔR) to the resistance in air (R_0). Response time (t_{90}) was set as the time taken to reach 90% of the maximum resistance change ($0.9\Delta R_{\text{max}}$).

References

1. Xie, L.S., Skorupskii, G., Dinca, M. Electrically conductive metal–organic frameworks. *Chem. Rev.* **120**, 8536-8580 (2020).
2. Sun, L., Campbell, M.G., Dinca, M. Electrically conductive porous metal-organic frameworks. *Angew. Chem., Int. Ed.* **55**, 3566-3579 (2016).
3. Hmadeh, M. *et al.* New porous crystals of extended metal-catecholates. *Chem. Mater.* **24**, 3511-3513 (2012).
4. Huang, X. *et al.* A two-dimensional pi-d conjugated coordination polymer with

- extremely high electrical conductivity and ambipolar transport behaviour. *Nat. Commun.* **6**, 7408 (2015).
5. Ko, M. Mendecki, L. Mirica, K.A. Conductive two-dimensional metal-organic frameworks as multifunctional materials. *Chem. Commun.* **54**, 7873-7891 (2018).
 6. Wu, G., Huang, J., Zang, Y., He, J., Xu, G. Porous field-effect transistors based on a semiconductive metal-organic framework. *J. Am. Chem. Soc.* **139**, 1360-1363 (2017).
 7. Sheberla, D., Bachman, J.C., Elias, J.S., Sun, C.J., Shao-Horn, Y., Dinca, M. Conductive MOF electrodes for stable supercapacitors with high areal capacitance. *Nat. Mater.* **16**, 220-224 (2017).
 8. Li, W.-H. *et al.* Conductive metal-organic framework nanowire array electrodes for high-performance solid-state supercapacitors. *Adv. Funct. Mater.* **27**, 1702067 (2017).
 9. Feng, D. *et al.* Robust and conductive two-dimensional metal-organic frameworks with exceptionally high volumetric and areal capacitance. *Nat. Energy* **3**, 30-36 (2018).
 10. Nam, K.W. *et al.* Conductive 2D metal-organic framework for high-performance cathodes in aqueous rechargeable zinc batteries. *Nat. Commun.* **10**, 4948 (2019).
 11. Koo, W.-T., Jang, J.-S., Kim, I.-D. Metal-organic frameworks for chemiresistive sensors. *Chem* **5**, 1938-1963 (2019).
 12. Campbell, M.G., Liu, S.F., Swager, T.M., Dinca, M. Chemiresistive sensor arrays from conductive 2D metal-organic frameworks. *J. Am. Chem. Soc.* **137**, 13780-13783 (2015).
 13. Smith, M.K., Mirica, K.A. Self-organized frameworks on textiles (SOFT): conductive fabrics for simultaneous sensing, capture, and filtration of gases. *J. Am. Chem. Soc.* **139**, 16759-16767 (2017).
 14. Yao, M.S. *et al.* Layer-by-layer assembled conductive metal-organic framework nanofilms for room-temperature chemiresistive sensing. *Angew. Chem., Int. Ed.* **56**, 16510-16514 (2017).
 15. Koo, W.-T., Kim, S.-J., Jang, J.-S., Kim, D.-H., Kim, I.-D. Catalytic metal nanoparticles embedded in conductive metal-organic frameworks for chemiresistors: highly active and conductive porous materials. *Adv. Sci.* **6**, 1900250 (2019).
 16. Choi, K.M., Na, K., Somorjai, G.A., Yaghi, O.M. Chemical environment control and enhanced catalytic performance of platinum nanoparticles embedded in nanocrystalline metal-organic frameworks. *J. Am. Chem. Soc.* **137**, 7810-7816 (2015).
 17. Wei, S. *et al.* Direct observation of noble metal nanoparticles transforming to thermally stable single atoms. *Nat. Nanotechnol.* **13**, 856-861 (2018).
 18. Li, G., Zhao, S., Zhang, Y., Tang, Z. Metal-organic frameworks encapsulating active nanoparticles as emerging composites for catalysis: Recent progress and perspectives. *Adv. Mater.* **30**, 1800702 (2018).
 19. Aulakh, D. *et al.* Direct imaging of isolated single-molecule magnets in metal-organic frameworks. *J. Am. Chem. Soc.* **141**, 2997-3005 (2019).
 20. Cai, D. *et al.* A highly conductive MOF of graphene analogue Ni₃HITP₂ as a sulfur host for high-performance lithium-sulfur batteries. *Small* **15**, 1902605 (2019).

21. Hoppe, B. *et al.* Graphene-like metal–organic frameworks: morphology control, optimization of thin film electrical conductivity and fast sensing applications. *CrystEngComm* **20**, 6458-6471 (2018).
22. Song, X. *et al.* 2D semiconducting metal-organic framework thin films for organic spin valves. *Angew. Chem., Int. Ed.* **59**, 1118-1123 (2020).
23. Rubio-Gimenez, V. *et al.* Bottom-up fabrication of semiconductive metal-organic framework ultrathin films. *Adv. Mater.* **30**, 1704291 (2018).
24. Yuan, K. *et al.* Construction of large-area ultrathin conductive metal-organic framework films through vapor-induced conversion. *Small* **15**, 1804845 (2019).
25. Campbell, M.G., Sheberla, D., Liu, S.F., Swager, T.M., Dinca, M. Cu₃(hexaiminotriphenylene)₂: an electrically conductive 2D metal-organic framework for chemiresistive sensing. *Angew. Chem., Int. Ed.* **54**, 4349-4352 (2015).
26. Lee, J.-C., Kim, J.-O., Lee, H.-J., Shin, B., Park, S. Meniscus-guided control of supersaturation for the crystallization of high quality metal organic framework thin films. *Chem. Mater.* **31**, 7377-7385 (2019).
27. Giri, G. *et al.* Tuning charge transport in solution-sheared organic semiconductors using lattice strain. *Nature* **480**, 504-508 (2011).
28. Kim, J.-O. *et al.* Inorganic polymer micropillar-based solution shearing of large-area organic semiconductor thin films with pillar-size-dependent crystal size. *Adv. Mater.* **30**, 1800647 (2018).
29. Echaide-Górriz, C., Clément, C., Cacho-Bailo, F., Téllez, C., Coronas, J. New strategies based on microfluidics for the synthesis of metal–organic frameworks and their membranes. *J. Mater. Chem. A* **6**, 5485-5506 (2018).
30. Faustini, M. *et al.* Microfluidic approach toward continuous and ultrafast synthesis of metal-organic framework crystals and hetero structures in confined microdroplets. *J. Am. Chem. Soc.* **135**, 14619-14626 (2013).
31. Wang, Y. *et al.* Bottom-up fabrication of ultrathin 2D Zr metal–organic framework nanosheets through a facile continuous microdroplet flow reaction. *Chem. Mater.* **30**, 3048-3059 (2018).
32. Kim, H., Min, K.I., Inoue, K., Im, D.J., Kim, D.P., Yoshida, J. Submillisecond organic synthesis: Outpacing Fries rearrangement through microfluidic rapid mixing. *Science* **352**, 691-694 (2016).
33. Gu, X., Shaw, L., Gu, K., Toney, M.F., Bao, Z. The meniscus-guided deposition of semiconducting polymers. *Nat. Commun.* **9**, 534 (2018).
34. Hao, J. *et al.* Synthesis of high-performance polycrystalline metal–organic framework membranes at room temperature in a few minutes. *J. Mater. Chem. A* **8**, 7633-7640 (2020).
35. Suryawanshi, P.L., Gumfekar, S.P., Kumar, P.R., Kale, B.B., Sonawane, S.H. Synthesis of ultra-small platinum nanoparticles in a continuous flow microreactor. *Colloid and Interface Sci. Commun.* **13**, 6-9 (2016).

36. Le Berre, M., Chen, Y., Baigl, D. From convective assembly to Landau-Levich deposition of multilayered phospholipid films of controlled thickness. *Langmuir* **25**, 2554-2557 (2009).
37. Potyrailo, R.A. Multivariable sensors for ubiquitous monitoring of gases in the era of internet of things and industrial internet. *Chem. Rev.* **116**, 11877-11923 (2016).
38. Kim, S.-J., Choi, S.-J., Jang, J.-S., Cho, H.-J., Kim, I.-D. Innovative nanosensor for disease diagnosis. *Acc. Chem. Res.* **50**, 1587-1596 (2017).
39. Loutfi, A., Coradeschi, S., Mani, G.K., Shankar, P., Rayappan, J.B.B. Electronic noses for food quality: A review. *J. Food. Eng.* **144**, 103-111 (2015).
40. Rubio-Giménez, V. *et al.* Origin of the chemiresistive response of ultrathin films of conductive metal-organic frameworks. *Angew. Chem., Int. Ed.* **130**, 15306-15310 (2018).
41. Choi, S.-J., Choi, H.-J., Koo, W.-T., Huh, D., Lee, H., Kim, I.-D. Metal-organic framework-templated PdO-Co₃O₄ nanocubes functionalized by SWCNTs: improved NO₂ reaction kinetics on flexible heating film. *ACS Appl. Mater. Interfaces* **9**, 40593-40603 (2017).
42. Rui, K. *et al.* Dual-function metal-organic framework-based wearable fibers for gas probing and energy storage. *ACS Appl. Mater. Interfaces* **10**, 2837-2842 (2018).
43. Chen, Z. *et al.* Mimicking a dog's nose: scrolling graphene nanosheets. *ACS Nano* **12**, 2521-2530 (2018).
44. Yuan, W., Liu, A., Huang, L., Li, C., Shi, G. High-performance NO₂ sensors based on chemically modified graphene. *Adv. Mater.* **25**, 766-771 (2013).
45. Yang, W., Wan, P., Zhou, X., Hu, J., Guan, Y., Feng, L. Additive-free synthesis of In₂O₃ cubes embedded into graphene sheets and their enhanced NO₂ sensing performance at room temperature. *ACS Appl. Mater. Interfaces* **6**, 21093-21100 (2014).
46. Cho, B. *et al.* Charge-transfer-based gas sensing using atomic-layer MoS₂. *Sci. Rep.* **5**, 8052 (2015).
47. Ko, K.Y. *et al.* Improvement of gas-sensing performance of large-area tungsten disulfide nanosheets by surface functionalization. *ACS Nano* **10**, 9287-9296 (2016).
48. Xu, T. *et al.* The ultra-high NO₂ response of ultra-thin WS₂ nanosheets synthesized by hydrothermal and calcination processes. *Sens. Actuators, B* **259**, 789-796 (2018).
49. Jaiswal, J., Sanger, A., Tiwari, P., Chandra, R. MoS₂ hybrid heterostructure thin film decorated with CdTe quantum dots for room temperature NO₂ gas sensor. *Sensors and Actuators B: Chemical* **305**, 127437 (2020).
50. Zhou, Y., Liu, G., Zhu, X., Guo, Y. Ultrasensitive NO₂ gas sensing based on rGO/MoS₂ nanocomposite film at low temperature. *Sens. Actuators, B* **251**, 280-290 (2017).

Acknowledgements

This work was supported by the National Research Foundation of Korea (NRF) grant funded

by the Korea government (MSIT) (2019R1A5A8080326) and (NRF-2018-Global Ph.D. Fellowship Program). This work is also supported by a grant from the Korea Institute of Energy Technology Evaluation and Planning (KETEP) and the Ministry of Trade Industry & Energy (MOTIE) of the Republic of Korea (No. 20183010014470). This work was supported by Nano Convergence Foundation funded by the Ministry of Science and ICT (MSIT, Korea) and the Ministry of Trade, Industry, and Energy (MOTIE, Korea) (project no.: 170720000230). This work was also supported by National Research Foundation (NRF) of the Korean Government (MSIT) (2020R1A2C301312711).

Author contributions

J.-O.K. and W.-T.K. conceived the concept and designed experiments. J.-O.K. fabricated the polyimide microfluidic device, MOF thin films and conducted structural characterization. W.-T.K. conducted sensing tests. H. Kim conducted CFD simulation and analysis with J.-O.K. C.P. assisted sensing measurements. C.A. Hutomo assisted MOF film fabrications. All authors contributed to the writing of the manuscript. All authors discussed the results and the manuscript. I.D.K. and S.P. were responsible for managing all aspects of this project.

Additional information

Supplementary information accompanies with the paper at doi: 10.XXX

Competing interests: The authors declare no competing financial interests.

Figures

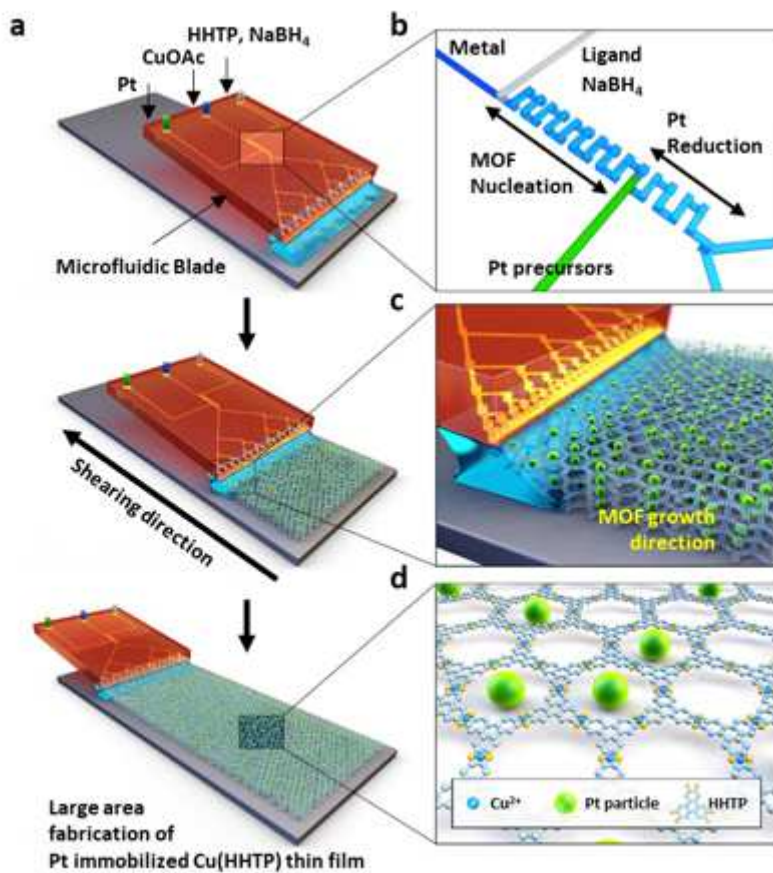


Figure 1

Fabrication of Pt@Cu₃(HHTP)₂ thin-film using MiCS. a, Schematic of Pt@Cu₃(HHTP)₂ MOF thin-film processing using microfluidic-based solution shearing process. CuOAc is copper(II) acetate. b, Schematic illustration of the microfluidic blade channel c, Schematic illustration of the MOF growth process using solution shearing. The nucleated Pt-particle embedded MOF solution is located between the microfluidic blade and the heated substrate. The MOF growth occurs at the edge of the meniscus. With the continuously supplying solution by the microfluidic blade during solution shearing, large-area and uniform Pt@Cu₃(HHTP)₂ thin-film can be formed. d, Crystal structure of Pt@Cu₃(HHTP)₂ thin-film (green sphere: Pt particle). @ means -embedded.

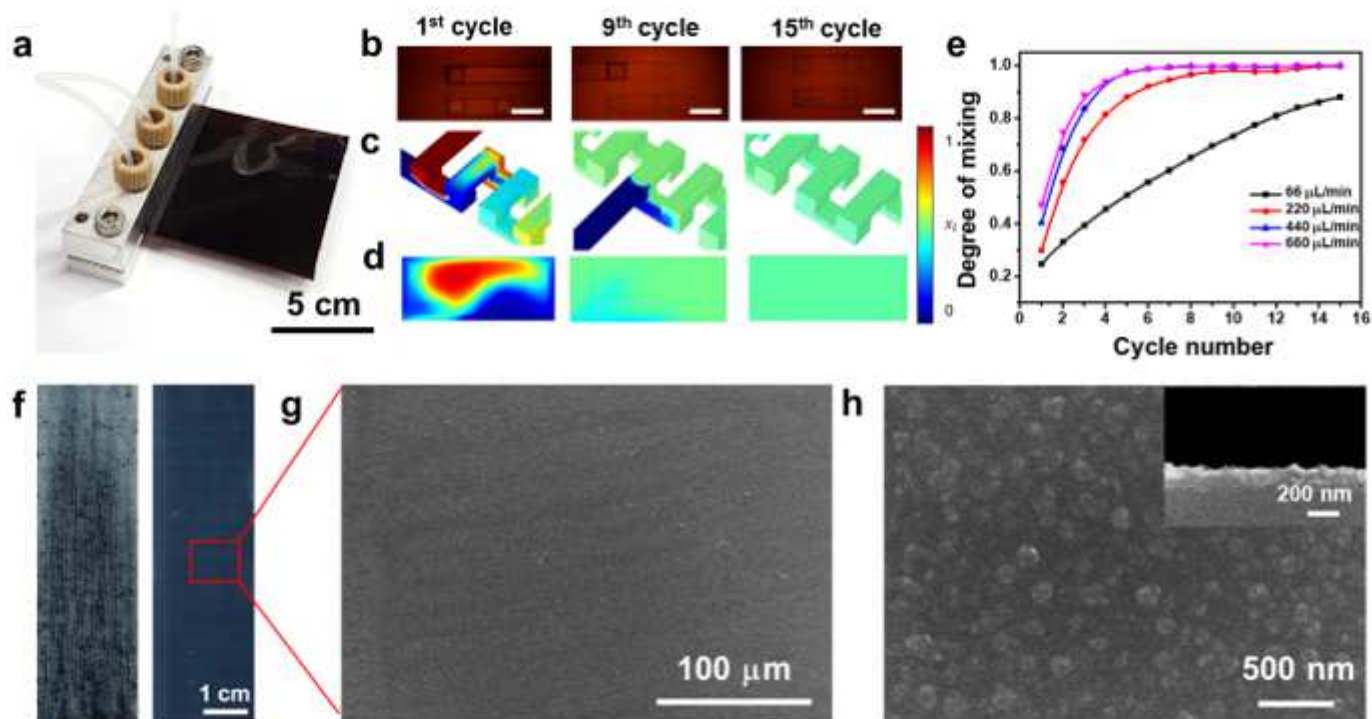


Figure 2

Characterization of MiCS.

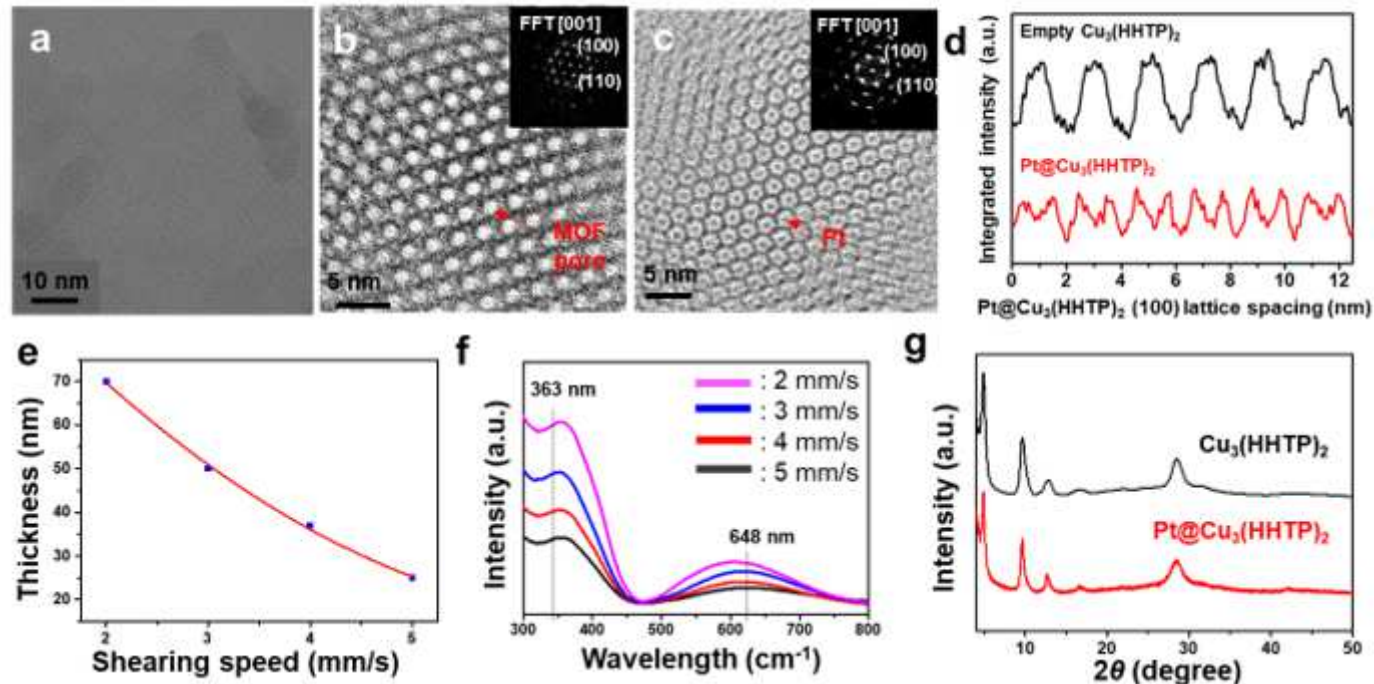


Figure 3

Characterization of Pt@C-MOF thin-films fabricated by MiCS. a-c, Cryo-TEM images of Pt@Cu₃(HHTP)₂: b, without Pt particle in the MOF pores. c, Pt particle immobilized in the MOF pores. d, Integrated intensity of Pt@Cu₃(HHTP)₂ plotted over 6 unit cells along the [100] direction, indicating a pattern when Pt particle

is introduced into the pores. e, Thickness control of Pt@Cu₃(HHTP)₂ thin-film via controlling the shearing speeds. f, UV-Vis spectrum of different thicknesses of Pt@Cu₃(HHTP)₂ thin-film. g, PXRD data of Cu₃(HHTP)₂ and Pt@Cu₃(HHTP)₂. @ means –embedded.

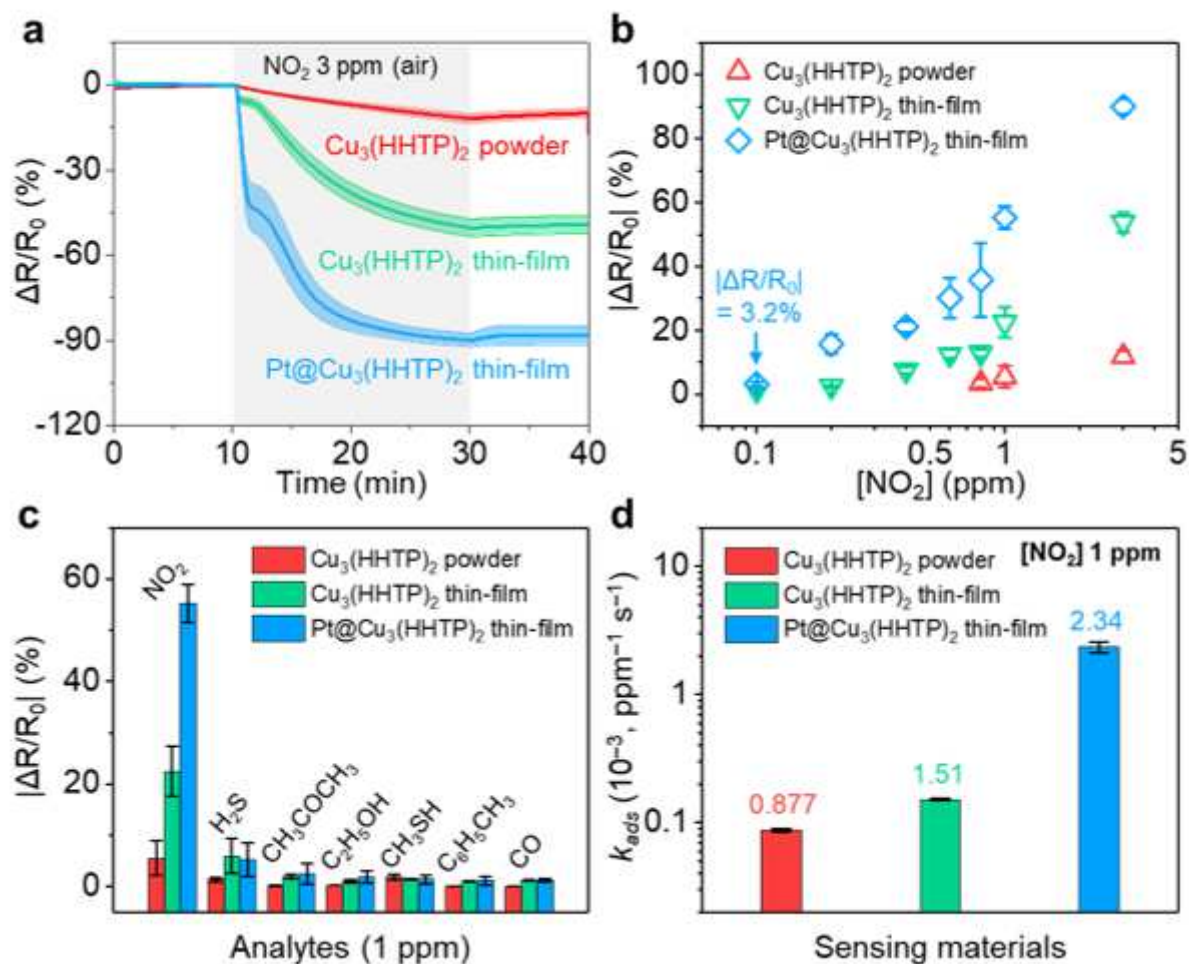


Figure 4

Sensing characteristics of Pt@Cu₃(HHTP)₂ thin-film. a, Resistance changes of Cu₃(HHTP)₂ powder, Cu₃(HHTP)₂ thin-film, and Pt@Cu₃(HHTP)₂ thin-film in response to 20 min exposure of NO₂ 3 ppm. The shaded areas present the standard deviation of the sensors (N ≥ 4). b, Normalized responses of the sensors to 0.1–3 ppm of NO₂. c, Selectivity of the sensors to 1 ppm of analytes. d, Calculated adsorption rate constants (k_{ads}) of the sensors. @ means –embedded.

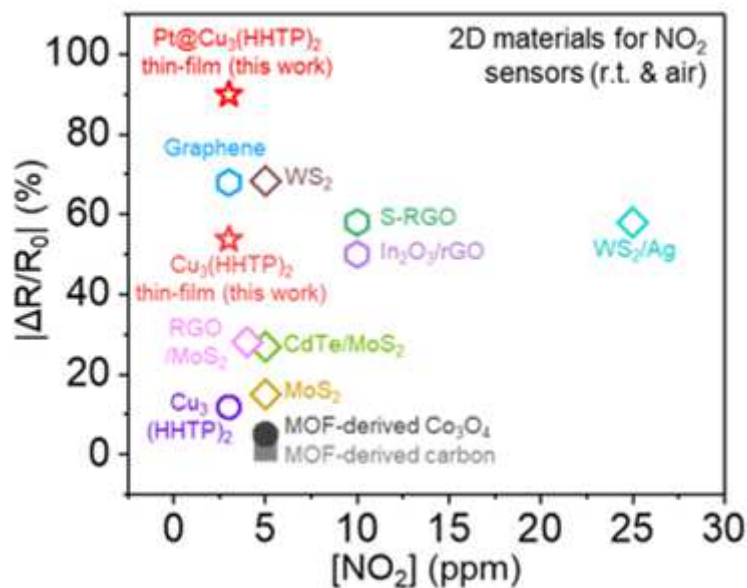


Figure 5

Comparison of the NO₂ responses of Pt@Cu₃(HHTP)₂ thin-film and Cu₃(HHTP)₂ thin-film with those of other materials. Other materials include Cu₃(HHTP)₂, graphene, WS₂, RGO/MoS₂ (RGO: reduced graphene oxide), CdTe/MoS₂, MoS₂, MOF-derived CO₃O₄, MOF-derived carbon, S-RGO (S-RGO: sulfonated RGO), In₂O₃/RGO, and WS₂/Ag.

Supplementary Files

This is a list of supplementary files associated with this preprint. Click to download.

- [Supportinginformation.docx](#)